A&A 648, A105 (2021)
https://doi.org/10.1051/0004-6361/202039125
© ESO 2021

Astronomy & Astrophysics

Looking through the photoionisation wake: Vela X−1 at $\varphi_{\rm orb} \approx 0.75$ with *Chandra*/HETG

R. Amato[1,2,3], V. Grinberg[3], N. Hell[4], S. Bianchi[5], C. Pinto[2], A. D'Aí[2], M. Del Santo[2], T. Mineo[2], and Santangelo[3]

[1] Dipartimento di Fisica e Chimica – Emilio Segrè, Università degli Studi di Palermo, via Archirafi, 36, 90123 Palermo, Italy
e-mail: astro.roberta@gmail.com
[2] INAF-IASF Palermo, via Ugo la Malfa, 153, 90146 Palermo, Italy
[3] Institute for Astronomy and Astrophysics (IAAT), University of Tübingen, Sand 1, 72076 Tübingen, Germany
[4] Lawrence Livermore National Laboratory, 7000 East Ave, Livermore, CA 94550, USA
[5] Dipartimento di Matematica e Fisica, Università degli Studi Roma Tre, Largo S. Leonardo Murialdo, 1, 00146 Roma, Italy

Received 7 August 2020 / Accepted 17 February 2021

ABSTRACT

Context. The supergiant X-ray binary Vela X−1 represents one of the best astrophysical sources to investigate the wind environment of an O/B star irradiated by an accreting neutron star. Previous studies and hydrodynamic simulations of the system have revealed a clumpy environment and the presence of two wakes: an accretion wake surrounding the compact object and a photoionisation wake trailing it along the orbit.
Aims. Our goal is to conduct, for the first time, high-resolution spectroscopy on *Chandra*/HETGS data at the orbital phase $\varphi_{\rm orb} \approx 0.75$, when the line of sight is crossing the photoionisation wake. We aim to conduct plasma diagnostics, inferring the structure and the geometry of the wind.
Methods. We performed a blind search employing a Bayesian block algorithm to find discrete spectral features and identify them thanks to the most recent laboratory results or through atomic databases. Plasma properties were inferred both with empirical techniques and with photoionisation models within CLOUDY and SPEX.
Results. We detect and identify five narrow radiative recombination continua (Mg XI-XII, Ne IX-X, O VIII) and several emission lines from Fe, S, Si, Mg, Ne, Al, and Na, including four He-like triplets (S XV, Si XIII, Mg XI, and Ne IX). Photoionisation models reproduce the overall spectrum well, except for the near-neutral fluorescence lines of Fe, S, and Si.
Conclusions. We conclude that the plasma is mainly photoionised, but more than one component is most likely present, which is consistent with a multi-phase plasma scenario, where denser and colder clumps of matter are embedded in the hot, photoionised wind of the companion star. Simulations with the future X-ray satellites *Athena* and XRISM show that a few hundred seconds of exposure is sufficient to disentangle the lines of the Fe Kα doublet and the He-like Fe XXV, improving, in general, the determination of the plasma parameters.

Key words. X-rays: binaries – stars: massive – stars: winds, outflows – line: identification – atomic processes – plasmas

1. Introduction

The eclipsing high-mass X-ray binary (HMXB) Vela X−1 (4U 0900-40) consists of a ∼283 s period pulsar (McClintock et al. 1976) and a blue supergiant companion star (HD 77851, a B0.5Ia class star, Hiltner et al. 1972). With an X-ray luminosity of $\sim 4\times10^{36}$ erg s^{-1} and a distance of 2 kpc from Earth (Giménez-García et al. 2016), it is one of the brightest HMXBs in the sky. It is a high inclination system (>73°, Joss & Rappaport 1984), with an orbital period of ∼8.9 d (Forman et al. 1973; Kreykenbohm et al. 2008) and an orbital separation of $\sim 53\,R_\odot$ (Quaintrell et al. 2003). The donor star has a radius of about $30\,R_\odot$ (Quaintrell et al. 2003), so that the pulsar is constantly embedded in the wind environment of the companion. The geometry of the accreting stream of matter onto the compact object is complex, being made up of an accretion wake, a photoionisation wake, and possibly a tidal stream, as both simulations (e.g., Blondin et al. 1990; Manousakis 2011) and observations in different wavebands show (e.g., Kaper et al. 1994; van Loon et al. 2001; Malacaria et al. 2016). A sketch of the binary system with the main features is given in Fig. 1. The line of sight intersects the different elements at different orbital phases, so that the observational data show strong changes in absorption along the whole orbital period (Doroshenko et al. 2013).

X-ray emission from Vela X−1 has already been detected and studied for several different orbital phases with different instruments (e.g., Haberl & White 1990; Goldstein et al. 2004; Watanabe et al. 2006; Fürst et al. 2010; Grinberg et al. 2017). High resolution X-ray studies of the system are of special interest, as they allow one to draw conclusions on the properties of the complex plasma. High-resolution data from the High-Energy Transmission Grating Spectrometer (HETGS; Canizares et al. 2005) of the *Chandra* X-ray Observatory (Weisskopf et al. 2000) of Vela X−1 during eclipse ($\varphi_{\rm orb} \approx 0$) were studied by Schulz et al. (2002), who discovered and identified a variety of emission features, including radiative recombination continua (RRCs) and fluorescent lines, which led to the idea of the coexistence of a hot optically thin photoionised plasma and a colder optically thick one. Goldstein et al. (2004) investigated *Chandra*/HETGS data

of the system at three different orbital phases ($\varphi_{\rm orb} \approx 0$, $\varphi_{\rm orb} \approx 0.25$, $\varphi_{\rm orb} \approx 0.5$), finding that the emission features revealed during the eclipse are obscured at $\varphi_{\rm orb} \approx 0.25$, but then they appear again at $\varphi_{\rm orb} \approx 0.5$, when the soft X-ray continuum diminishes. The simultaneous presence of H- and He-like emission lines and fluorescent lines of near-neutral ions can be explained by contributions from different regions: The warm photoionised wind of the companion star and smaller cooler regions, or clumps, of gas. Watanabe et al. (2006) compared the same *Chandra*/HETGS data sets to 3D Monte Carlo simulations of X-ray photons propagating through a smooth, undisturbed wind. Based on this assumption, they deducted that highly ionised ions, which give rise to emission lines, are mainly located in the region between the neutron star (NS) and the companion star, while the fluorescent lines are produced in the extended stellar wind, from reflection of the stellar photosphere, and in the accretion wake. More recent results on the same orbital phase by Odaka et al. (2013) with Suzaku and by Martínez-Núñez et al. (2014) with *XMM-Newton*, respectively, highlight flux variability and strong changes in absorption over periods of the order of kiloseconds. The same variability is found in *Chandra*/HETGS data at $\varphi_{\rm orb} \approx 0.25$ from Grinberg et al. (2017), who attribute the changes in the overall absorption to the clumpy nature of the winds from the companion. Moreover, the high energy resolution of *Chandra* allowed for the detection of line emission features from several ionised elements, corroborating the idea of a co-existence of cool and hot gas phases in the system.

Hydrodynamic simulations (Manousakis & Walter 2015; El Mellah et al. 2018, 2019) suggest the presence of a more complex structure around the neutron star (NS), with a bow shock and eventually the formation of a transient wind-captured accretion disk (Liao et al. 2020). Such features can influence the way clumps accrete onto the compact objects, reducing the amount of transferred angular momentum or introducing time lags and phase mixing when the clumps are stored in such structures.

In this work we present, for the first time, a high-resolution spectroscopic study of *Chandra*/HETG archival data of Vela X−1 at orbital phase $\varphi_{\rm orb} \approx 0.75$, that is, when the line of sight intersects the photoionisation wake (see Fig. 1). The study of the X-ray spectrum at this specific orbital phase, where the absorption from the wind of the X-rays coming from the NS is high, allows for the detection of a large number of lines from different elements in high ionisation states and, thus, the application of plasma diagnostic techniques to characterise the accretion environment. The paper is structured as follows: We first look for changes in the hardness of the flux in Sect. 2, finding none; then we proceed with a blind search for spectroscopic absorption and emission features, applying a Bayesian block (BB) algorithm to the unbinned spectrum; we present the identification of all the detected features in Sect. 3, while in Sect. 4 we compare the observational data with two different photoionisation codes; in Sect. 5 we discuss the plasma properties and the geometry of the wind of the companion star; in Sect. 6 we perform simulations with future X-ray satellites; and we present our conclusions in Sect. 7.

2. Data reduction and temporal analysis

We analysed the high energy grating (HEG) and medium energy grating (MEG) data sets of the *Chandra*/HETG ObsID 14654, taken on 2013 July 30, with ACIS-S, in FAINT mode, for a total exposure time of 45.88 ks. According to the ephemeris of Kreykenbohm et al. (2008), the data set covers the orbital phase of $\varphi_{\rm orb} = 0.72$–0.78, where $\varphi_{\rm orb} = 0$ is defined as mid-eclipse. Data were reprocessed using CIAO 4.11, with CALDB 4.8.2. We followed the standard *Chandra* data analysis threads, but we chose a narrower sky mask to avoid the overlapping of the extraction region and to improve the flux at the shortest wavelengths.

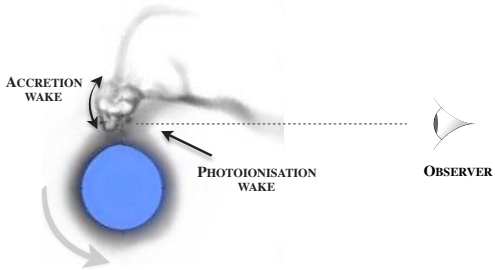

Fig. 1. Sketch of Vela X−1 from Grinberg et al. (2017) showing the accretion and photoionisation wakes. The blue circle represents the donor star HD 77851, while the pulsar is hidden in the accretion wake. The grey arrow indicates the verse of the rotation of the binary system. At the orbital phase $\varphi_{\rm orb} \approx 0.75$, the observer is looking at the system from the right, so that the line of sight (dashed line) is crossing the photoionisation wake.

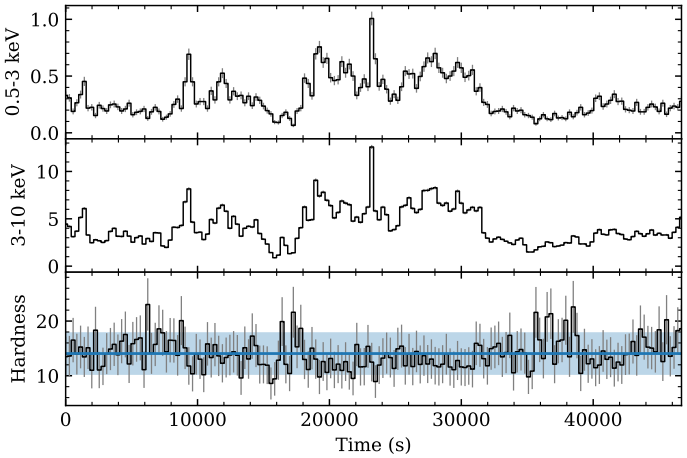

Fig. 2. Light curves in units of counts s^{-1} in the soft 0.5–3 keV (*top panel*) and hard 3–10 keV (*middle panel*) energy bands, and corresponding hardness ratio ((3–10 keV)/(0.5–3 keV) *bottom panel*). The blue horizontal line indicates the mean value of the hardness ratio, with the 1σ uncertainty given by the blue area. Data were binned to the spin period of 238 s, error bars at 1σ.

Following the work of Grinberg et al. (2017), who observed a change in the hardness of the source during phase $\varphi_{\rm orb} \approx 0.25$, we extracted the light curve in two different energy bands, 0.5–3 keV (soft) and 3–10 keV (hard), and computed the hardness ratio, defined as the ratio between the counts in the hard and soft bands. Figure 2 shows the result, with data binned to the neutron star spin period of 283 s (errors at 1σ). The hardness ratio values at $\varphi_{\rm orb} \approx 0.75$ are higher than the ones obtained by Grinberg et al. (2017) by at least a factor of ten, which is not surprising considering the high absorption expected at this orbital phase. Moreover, the hardness ratio is almost flat for the whole observation, which is in contrast to Grinberg et al. (2017), where a variability of a factor of three was observed. Hence, we extracted only one spectrum in the full energy range of 0.5–10 keV (Fig. 3).

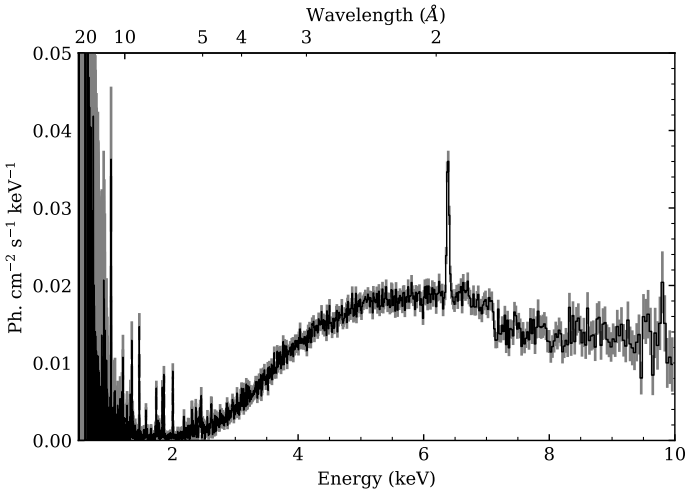

Fig. 3. Combined HEG and MEG spectrum of *Chandra* ObsID 14654 in the energy range of 0.5–10 keV.

3. High-resolution spectroscopy

We used the Interactive Spectral Interpretation System (ISIS) 1.6.2-43 (Noble & Nowak 2008) to perform the spectroscopic analysis of the data, with the ISIS functions (ISISscripts) provided by the ECAP/Remeis observatory and MIT[1], cross sections from Verner et al. (1996), and solar abundances from Wilms et al. (2000). We used the Cash statistic (Cash 1979) with the spectrum binned to the MEG resolution. All uncertainties are given at 90% confidence level.

We performed a blind search of spectral features, using a BB algorithm (Scargle et al. 2013), as described in Young et al. (2007) and as applied to *Chandra*/HETGS data by Grinberg et al. (2017). To optimise the line detection algorithm, we divided the whole spectrum into five regions of interest, named after the most significant element detected in each of them, as reported in Table 1. These spectral regions were analysed one by one. We locally modelled the continuum with a simple power law and then looked for significant deviations in the residuals. Given the narrow wavelength ranges of individual regions, the continuum is always adequately well fitted by a power law. Similar piecewise approaches have been previously used for line searches and modelling repeatedly (see, e.g., Yao et al. 2008; van den Eijnden et al. 2019).

The BB algorithm determines whether a data point is far from the model above a certain significant threshold, defined by a parameter, α, such that each detection has a significance of $p \sim \exp(-2\alpha)$, corresponding to a probability of $P \sim 1 - \exp(-2\alpha)$ of positive detection. For each new detection, we added one or more Gaussian components to the model for emission and absorption lines and the XSPEC (Arnaud 1996) functions `redge` and `edge` for the RRCs and the Fe K-edge (Sects. 3.1 and 5.1), respectively. After each addition, we fitted the data and applied the algorithm once more. We iterated the process until the significance dropped to 95%, corresponding to $\alpha \sim 1.5$. All the line detections with their corresponding values of α are listed in Tables 2–6, while Table 1 shows the best-fit values of the power law parameters for each spectral region and the goodness of the fit. Table 7 displays the best-fit values of the RRCs.

In some cases, lines that are too close to be clearly resolved by the algorithm, such as for He-like triplets, are detected as a single block. In such cases, we used our knowledge of atomic physics to add the proper number of lines to the model. Moreover, to improve the fit, we fixed the distance of known lines, since the BB per se is a blind algorithm, that is, it does not take into account known line distances. We did this for the H-like Lyα and Lyβ lines (Erickson 1977) and the He-like triplets (Drake 1988), assuming that Doppler shifts are the same within the same ionic species.

Whenever a line appeared unresolved, we fixed its width to 0.003 Å, corresponding to about one-third of the MEG resolution (0.023 Å FWHM)[2]. Line identification for S and Si ions accounts for the most recent laboratory measurements from Hell et al. (2016), while for the other elements, we used the AtomDB database[3] (Foster et al. 2012, 2017).

For every detected He-triplet, we computed the density-sensitive ratio $R = f/i$ and the temperature-sensitive ratio $G = (i+f)/r$, where f is the intensity of the forbidden line (1s2s ^{3}S$_1$–1s^2 ^{1}S$_0$), i is the intensity of the intercombination line (1s2p ^{3}P$_1$–1s^2 ^{1}S$_0$), and r is the intensity of the resonant line (1s2p ^{1}P$_1$–1s^2 ^{1}S$_0$) (Gabriel & Jordan 1969; Porquet & Dubau 2000)[4]. In our case, the intensities of the lines are linked to reproduce G and R as free parameters in the fit. Results are reported in Table 8. In the following subsections, we present in detail the results of the BB procedure for each spectral region of interest.

3.1. Iron region

In the Fe region (wavelength range 1.6–2.5 Å, cf. Table 1), the BB method found only one strong line, which we identified with Fe Kα and one edge, identified with the Fe K-edge (see Fig. 4). Best-fit values for these features are reported in Table 2. Although the strong Fe Kα line implies the presence of a strong Fe Kβ component, our approach did not detect it. We discuss the possible reasons in Sect. 5.

Given the overall strength of the Fe Kα line, we attempted an additional fit, letting the line width free. We obtained a best-fit value of $\sigma = \left(3.4^{+0.9}_{-1.1}\right) \times 10^{-3}$ Å, consistent with our previous assumption and with the results of Tzanavaris & Yaqoob (2018).

3.2. Sulphur region

We studied the S region in the wavelength range of 4.5–6.0 Å (Table 1). Line identification is based on the recent laboratory measurements from Hell et al. (2016). The BB algorithm detected a single block between 5 Å and 5.4 Å, with $\alpha = 27$. We modelled this block with the S XV He-like triplet, the S XIV, the S XI, and the blended fluorescence S II-VIII lines. The second run of the algorithm resulted in the detection of the S XVI Lyα, with $\alpha = 12$. Lastly, the following three more lines were detected: the Si XIII Heβ ($\alpha = 8$), the S IX ($\alpha = 2.7$), and an unidentified absorption line at ~5.457 Å ($\alpha = 2.2$). No reference wavelength was found for this last absorption line. Considering the low value of the parameter α and the lack of any other absorption feature in the whole spectrum, it is most likely that the line is just a statistical fluctuation.

[1] http://www.sternwarte.uni-erlangen.de/isis/

[2] http://cxc.harvard.edu/cdo/about_chandra

[3] http://www.atomdb.org/index.php

[4] Gabriel (1972) referred to the transitions of the lines of the He-like triplets as w for the resonant line, x and y for the two components of the intercombination line, and z for the forbidden line. With this notation, the ratios for plasma diagnostic are expressed as $R = z/(x+y)$ and $G = (z + (x+y))/w$.

Table 1. Best-fit values of the power laws used to model the continuum and values of the Cash statistic per degrees of freedom (d.o.f.) for each region of the spectrum.

Region	Wavelength range (Å)	Γ	Norm. (keV s^{-1} cm^{-2})	Cash(d.o.f.)
Fe	1.6–2.5	$-0.082^{+0.004}_{-0.008}$	$0.0158^{+0.0023}_{-0.0018}$	1.03(179)
S	4.5–6.0	-5.38 ± 0.05	$\left(1.04^{+0.06}_{-0.16}\right) \times 10^{-5}$	1.14(279)
Si	6.0–7.4	-0.3 ± 0.1	$(3.4 \pm 0.2) \times 10^{-4}$	1.19(247)
Mg	7.5–10.0	$2.31^{+0.15}_{-0.16}$	$(1.27 \pm 0.07) \times 10^{-3}$	1.26(468)
Ne	10.0–14.5	0.1 ± 0.7	$\left(6.9^{+0.7}_{-0.6}\right) \times 10^{-4}$	0.99(892)

Table 2. Features detected in the Fe region (1.6–2.5 Å) with the detection parameter α and the best-fit values.

Line	BB α	Ref. wavelength (Å)	Det. wavelength (Å)	Line flux (ph s^{-1} cm^{-2} $\times 10^{-4}$)	τ
Fe Kα	157	1.9375 [(a)]	1.9388 ± 0.0006	9.4 ± 0.8	–
Fe K edge	47	1.7433 [(b)]	1.742 ± 0.003	–	0.31 ± 0.03

Notes. The width of the Fe Kα line was fixed to 0.003 Å. [(a)]Drake (1988). [(b)]Bearden & Burr (1967).

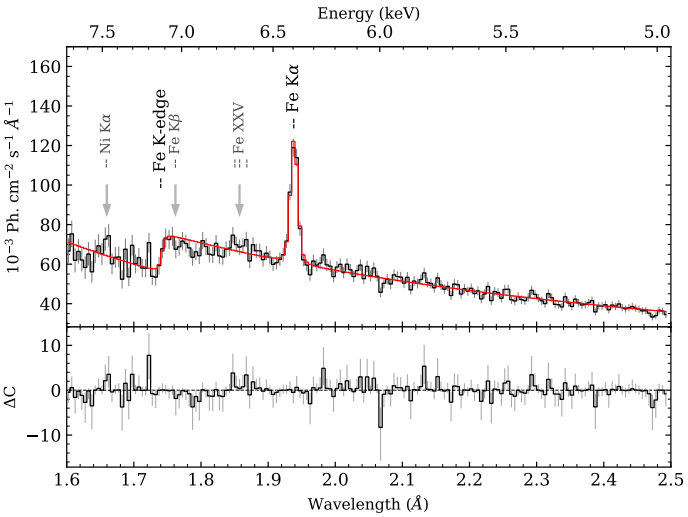

Fig. 4. Fe-region spectrum and best-fit model (red line), with residuals shown in the bottom panel. The only line detected by the BB algorithm is identified and marked as a FeKα emission line, as well as the detected Fe K-edge. Arrows mark the position of the expected Ni Kα, Fe Kβ, and He-like Fe XXV lines (in grey).

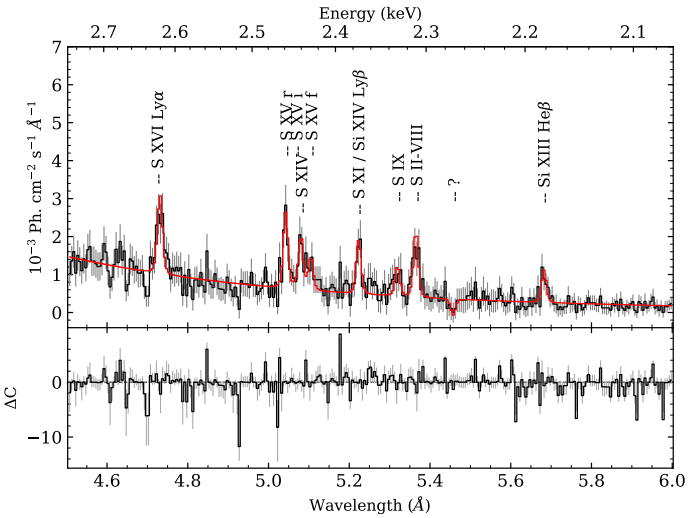

Fig. 5. S-region spectrum and best-fit model (red line), with residuals shown in the *bottom panel*. The detected lines are labelled if identified.

In the same region, we could also expect to find the Si XIV Lyβ line at 5.217 Å (Erickson 1977). The lack of a significant detection of this line is probably due to the strong continuum. However, since the Si XIV Lyα line is strong in the Si region (see Sect. 3.3), the Si XIV Lyβ is most likely present and blended with the S XI line. In Fig. 5, we marked the line at 5.224 Å with both its possible identifications. Given this line confusion, the Lyβ/Lyα ratio for Si XIV cannot be easily constrained. Only an upper limit of 0.55 can be derived, assuming the minimum flux for Lyα (cf. Sect. 3.3) and that the entire flux of the discussed blend is due to Si XIV Lyβ. Moreover, the high absorption constitutes a source of additional uncertainty as it influences the line ratio (Kaastra & Mewe 1995).

For this region, all the line widths were fixed to 0.003 Å. Best-fit values are reported in Table 3, together with the Doppler velocities computed with respect to laboratory reference values (Hell et al. 2016). Figure 5 shows the spectrum, the best-fit model and the residuals of the fit. From the S XV triplet, we obtained the best fit ratios $R = 9.9^{+2.4}_{-2.2}$ and $G = 0.48^{+0.14}_{-0.10}$ (Table 8).

3.3. Silicon region

We searched for Si lines in the region 6.0–7.4 Å (Table 1). At the first trial ($\alpha = 190$), the BB algorithm highlighted the Si XIV Lyα line and a whole block in the range of 6.6–6.8 Å, which we modelled with the He-like triplet Si XIII at first. The fluorescent line blend Si II-VI is detected with $\alpha = 121$, while a whole block is detected at the wavelengths 6.9-7.1 Å, with $\alpha = 32$. We added three Gaussians to model this block, according to the laboratory measurements by Hell et al. (2016) (see also Grinberg et al. 2017), corresponding to the Si VII, Si VIII, and Si IX lines. The last detections are identified as the Al XIII Lyα line ($\alpha = 9$), the Si X and Si XI lines ($\alpha = 5$), and the Si XII line ($\alpha = 1.8$).

Table 3. Spectral features detected in the S region.

Line	BB α	Ref. wavelength (Å)	Det. wavelength (Å)	Line flux (ph s^{-1} cm^{-2} $\times 10^{-5}$)	Velocity (km s^{-1})
S XVI Lyα	12	4.7329 [(a)]	4.731 ± 0.003	$3.5^{+1.0}_{-0.9}$	-50^{+180}_{-170}
S XV r	27	5.0386	$5.0422^{+0.0018}_{-0.0014}$	$3.18^{+1.07}_{-0.99}$	210^{+110}_{-80}
S XV i	27	5.0666	$5.0682^{+0.0018}_{-0.0014}$ [(b)]	0.14 ± 0.03	$= v_{(\mathrm{S_{XV}}\,r)}$
S XV f	27	5.1013	$5.1049^{+0.0018}_{-0.0014}$ [(b)]	$0.06^{+0.04}_{-0.07}$	$= v_{(\mathrm{S_{XV}}\,r)}$
S XIV	27	5.0858	5.081 ± 0.003	2.3 ± 0.8	-310^{+180}_{-160}
S XI/Si XIV Lyβ [(c)]	27	5.2250	5.224 ± 0.002	$2.3^{+0.8}_{-0.7}$	-70 ± 140
S IX	2.7	5.3163	$5.320^{+0.006}_{-0.009}$	$1.3^{+0.8}_{-0.7}$	210^{+340}_{-510}
S II-VIII	27	5.3616	5.365 ± 0.003	$2.8^{+0.9}_{-0.8}$	200 ± 150
	2.2	–	$5.457^{+0.002}_{-0.003}$	$-0.69^{+0.011}_{-0.24}$	–
Si XIII Heβ	8	5.681 [(d)]	5.683 ± 0.003	$1.4^{+0.6}_{-0.5}$	80^{+150}_{-160}

Notes. For each feature we report the detection parameter α, the best-fit values (wavelength and line flux), and the Doppler velocities, computed using reference wavelengths measured by Hell et al. (2016). Line widths were fixed to 0.003 Å for all the lines. Hell et al. (2016) reports the statistical uncertainties for each energy, which correspond to an error in wavelength of the order of 10^{-4}–10^{-5} Å. However, the authors state that there is also a systematic uncertainty of 0.23 eV for S lines, which results in an error on the wavelength of 0.0008 Å. [(a)]Garcia & Mack ((1965). [(b)]Distances between the r line and the i and f lines computed from Drake (1988). [(c)]The reference wavelength of Si XIV Lyβ is 5.217 Å (Erickson 1977). [(d)]Kelly (1987).

In the same region, also the RRC of Mg XII is detected at 6.321 Å (1.961 ± 0.002 keV), with a temperature of $4.5^{+5.8}_{-2.5}$ eV. Lastly, we added one more `redge` function to model the Mg XI RRC, expected at 7.037 Å (Drake 1988). It results in a temperature of $3.1^{+1.6}_{-1.1}$ eV, which is consistent with the one of Mg XII RRC (Table 7).

The width of the lines was fixed to 0.003 Å, except for the Si XIV Lyα line, which has a slightly larger width of $\left(7.3^{+1.2}_{-1.1}\right) \times 10^{-3}$ Å. For each line, we computed the Doppler velocities with respect to the laboratory or literature reference wavelengths. All the best-fit values of the emission lines and RRCs are reported in Tables 4 and 7, respectively, while the spectrum, the best-fit model, and the residuals are shown in Fig. 6. The best fit values of the R and G ratios of the S XIII triplet resulted in $R = 6.0 \pm 0.6$ and $G = 0.80^{+0.10}_{-0.09}$ (Table 8). The BB algorithm did not detect the Mg XII Lyβ emission line expected at ~7.1037 Å (Erickson 1977). Also in this case the line is most likely embedded in the (near-)neutral fluorescence Si II-VI lines.

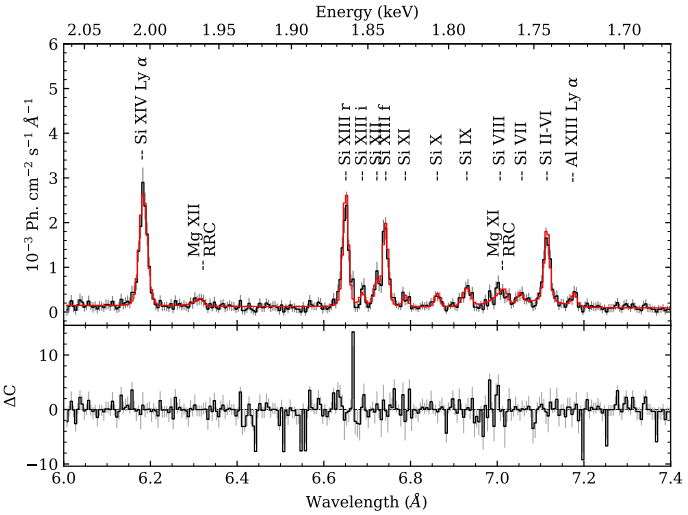

Fig. 6. Si-region spectrum and best-fit model (red line), with residuals shown in the *bottom panel*.

3.4. Magnesium region

The region that we took into account to look for Mg emission lines ranges from 7.5 Å to 10 Å (Table 1). The first line detected corresponds to the Mg XII Lyα ($\alpha = 220$). The successive detection ($\alpha = 89$) consisted in a block in the range of ~9–9.4 Å, which we modelled with three Gaussians for the He-like triplet Mg XI. In the same block, we inserted the Ne X RRC (Schulz et al. 2002; Watanabe et al. 2006; Goldstein et al. 2004). We also detected and identified the Mg XI Heβ ($\alpha = 48$), the Ne X Lyγ ($\alpha = 15$), the Al XII r Heα ($\alpha = 7$), the Ne X Heδ ($\alpha = 4.4$), the Fe XX ($\alpha = 3.4$), and the Fe XXIV ($\alpha = 2.9$) emission lines. Best-fit values are reported in Table 5, while the spectrum, the best-fit model, and the residuals are shown in Fig. 7. A few lines show a broadening that required to let their widths free. This is the case for Mg XII Lyα whose width of $(7.4 \pm 1.2) \times 10^{-3}$ Å is in agreement with those of Si XIV (Sect. 3.3) and Ne X Lyα (Sect. 3.5) lines. Other broadened lines are the Mg XI r and the Ne X Heδ, ~0.01 Å width, and a Fe XXIII line (~0.025 Å width). The Ne X RRC, at a wavelength of ~9.116 Å ($1.3600^{+0.0012}_{-0.0010}$ keV), indicates a temperature of $10.8^{+3.4}_{-2.5}$ eV (Table 7), which is consistent with previous findings at different orbital phases (Schulz et al. 2002; Goldstein et al. 2004). Doppler shifts of the Lyα, the Heβ, and the triplet lines are around 150 km s^{-1}. From the intensities of the Mg XI triplet, we obtained the ratios $R = 1.20^{+0.25}_{-0.23}$ and $G = 0.74^{+0.13}_{-0.14}$ (Table 8) for plasma diagnostic.

3.5. Neon region

The region for Ne emission lines goes from 10 Å to 14.5 Å (Table 1). We detected and identified 11 lines and two RRCs. Best-fit values are reported in Tables 6 and 7; the spectrum, best-fit model, and residuals are shown in Fig. 8. The first line to be detected by the BB procedure ($\alpha = 49$) was the Ne X Lyα at a wavelength of 12.1398 Å and with a width of $(9.6^{+3.0}_{-2.8}) \times 10^{-3}$ Å.

Table 4. Spectral features detected in the Si region.

Line	BB α	Ref. wavelength (Å)	Det. wavelength (Å)	Line flux (ph s^{-1} cm^{-2} $\times 10^{-5}$)	Velocity (km s^{-1})
Si XIV Lyα	190	6.1817 [(a)]	6.184 ± 0.001	6.2 ± 0.6 [(b)]	100 ± 50
Si XIII r	190	6.6483	6.6506 ± 0.0007	$4.5^{+0.8}_{-0.7}$	100 ± 30
Si XIII i	190	6.7195	6.6887 ± 0.0007 [(c)]	$0.51^{+0.05}_{-0.04}$	$= v_{(\mathrm{Si\,XIII}\,r)}$
Si XIII f	190	6.7405	6.7427 ± 0.0007 [(c)]	3.1 ± 0.4	$= v_{(\mathrm{Si\,XIII}\,r)}$
Si XII	1.8	6.7197	6.722 ± 0.003	0.9 ± 0.3	110 ± 110
Si XI	5	6.7841	6.788 ± 0.004	$0.42^{+0.18}_{-0.16}$	170 ± 180
Si X	5	6.8558	6.862 ± 0.004	$0.49^{+0.19}_{-0.17}$	270 ± 180
Si IX	32	6.9279	6.930 ± 0.003	1.1 ± 0.3	80 ± 120
Si VIII	32	7.0008	7.006 ± 0.005	1.6 ± 0.3	220 ± 210
Si VII	32	7.0577	$7.057^{+0.005}_{-0.004}$	0.5 ± 0.2	-40^{+210}_{-170}
Si II-VI [(d)]	121	7.1172	7.115 ± 0.001	2.6 ± 0.4	-120 ± 40
Al XIII Lyα	9	7.1764 [(e)]	7.177 ± 0.003	0.6 ± 0.2	20^{+110}_{-120}

Notes. For each of them, we report the detection parameter α and the best-fit values (wavelength and line flux). Line widths were fixed to 0.003 Å if not stated otherwise. Doppler velocities of the Si lines were computed with respect to the reference wavelengths measured by Hell et al. (2016). Hell et al. (2016) report a systematic uncertainty of 0.13 eV for Si lines, corresponding to an error on the wavelength of 0.0005 Å. [(a)]Garcia & Mack ((1965). [(b)]This line results in a best line width of $7.3^{+1.2}_{-1.1} \times 10^{-3}$ Å. [(c)]Distances between the r line and the i and f lines computed from Drake (1988). [(d)]The Mg Lyβ (7.1037 Å, Erickson 1977) might be blended with the Si II-VI line. [(e)]Erickson (1977).

Table 5. Spectral features detected in the Mg region (7.5–10 Å).

Line	BB α	Ref. wavelength (Å)	Det. wavelength (Å)	Line flux (ph s^{-1} cm^{-2} $\times 10^{-5}$)	Velocity (km s^{-1})
Al XII Heα	7	7.7573 [(a)]	$7.782^{+0.012}_{-0.011}$	0.9 ± 0.3 [(b)]	960^{+460}_{-430}
Mg XI Heβ	48	7.850 [(c)]	7.8565 ± 0.0017	1.2 ± 0.3	250 ± 70
Fe XXIV	2.9	7.985 [(d)]	$7.980^{+0.008}_{-0.005}$	$0.30^{+0.17}_{-0.14}$	-190^{+300}_{-190}
Mg XII Lyα	220	8.42101 [(e)]	8.4226 ± 0.0011	$5.3^{+0.6}_{-0.5}$ [(f)]	180 ± 40
Mg XI r	89	9.16896 [(a)]	9.1728 ± 0.0015	3.7 ± 0.8 [(g)]	130 ± 50
Mg XI i	89	9.2312 [(a)]	9.2343 ± 0.0015 [(a)]	$1.51^{+0.14}_{-0.23}$	$= v_{(\mathrm{Mg\,XI}\,r)}$
Mg XI f	89	9.3143 [(a)]	9.3188 ± 0.0015 [(a)]	1.5 ± 0.4	$= v_{(\mathrm{Mg\,XI}\,r)}$
Fe XX [(h)]	3.4	9.282 [(i)]	9.290 ± 0.004	1.0 ± 0.4	260 ± 130
Ne X Lyδ	4.4	9.481 [(e)]	9.485 ± 0.006	0.6 ± 0.3	130 ± 190
Ne X Lyγ	15	9.708 [(e)]	9.708 ± 0.005	$1.3^{+0.5}_{-0.4}$ [(j)]	0 ± 150

Notes. For each of them, we report the detection parameter α, the best-fit values (wavelength and line flux), and the Doppler velocities, computed with respect to the reference wavelength from the literature. Line widths were fixed to 0.003 Å if not stated otherwise. [(a)]Drake (1988). [(b)]Line width of $0.025^{+0.012}_{-0.008}$ Å. [(c)]Kelly (1987). [(d)]Wargelin et al. (1998). [(e)]Erickson (1977). [(f)]For this line, the best-fit line width value was $(7.4 \pm 1.2) \times 10^{-3}$ Å. [(g)]Line width of 0.011 ± 0.003 Å. [(h)]Close to the same wavelength, there is also the Ne X Lyζ emission line at 9.291 Å, but with a lower intensity ratio. In this case, the resulting Doppler velocity would be (-32 ± 129) km s^{-1}. [(i)]Reference wavelength from AtomDB. [(j)]Line width of $0.010^{+0.005}_{-0.004}$ Å.

The successive detection ($\alpha = 29$) was a line at ~10.24 Å, which we identified with the Ne X Lyβ. Hence, we fixed the distance of the latter line with respect to the corresponding Lyα according to Erickson (1977). The next detection ($\alpha = 17$) was a block from 13.4 Å to 13.9 Å, which we modelled with the Ne IX triplet (Grinberg et al. 2017; Goldstein et al. 2004; Watanabe et al. 2006). Lastly, we detected six more lines, corresponding to Ne IX Heβ at 11.549 Å ($\alpha = 8$), Ne IX Heγ at 11.005 Å ($\alpha = 7$), Ne IX Heε at 10.644 Å ($\alpha = 3.2$), Na XI Lyα at 10.023 Å ($\alpha = 2.5$), Fe XIX at 10.814 Å ($\alpha = 1.8$), and Fe XXI at 12.285 Å ($\alpha = 1.7$). The Ne IX RRC at 10.374 Å was detected with $\alpha = 8$ and resulted in a best-fit temperature of $4.5^{+3.4}_{-2.1}$ eV, while the O VIII RRC at 14.22 Å was detected with $\alpha = 2.8$ with a best-fit temperature of $0.9^{+4.2}_{-0.6}$ eV (Table 7). This is the first detection of the O VIII RRC in *Chandra* data for Vela X−1. It was implied in ASCA observations (Sako et al. 1999), suggested by Schulz et al. (2002), and only recently detected using *XMM-Newton* data (Lomaeva et al. 2020). We note that the O VIII RRC might also be blended with a Fe XVIII line at 14.208 Å (Brown et al. 1998).

We computed Doppler shifts for all the lines, obtaining velocities consistent with each other (Table 6). The intensities of the lines of the Ne IX triplet gave diagnostic best fit ratios of $R = 1.2^{+0.6}_{-0.5}$ and $G = 3.7^{+4.4}_{-1.7}$ (Table 8).

4. Photoionisation models with CLOUDY and SPEX

We attempted a more physical modelling of the detected features using photoionisation models with the latest release of CLOUDY (Ferland et al. 2017; Chakraborty et al. 2020) and SPEX (v3.05, Kaastra et al. 1996, 2018). In both cases, we used proto-Solar abundances from Lodders et al. (2009). Both of these

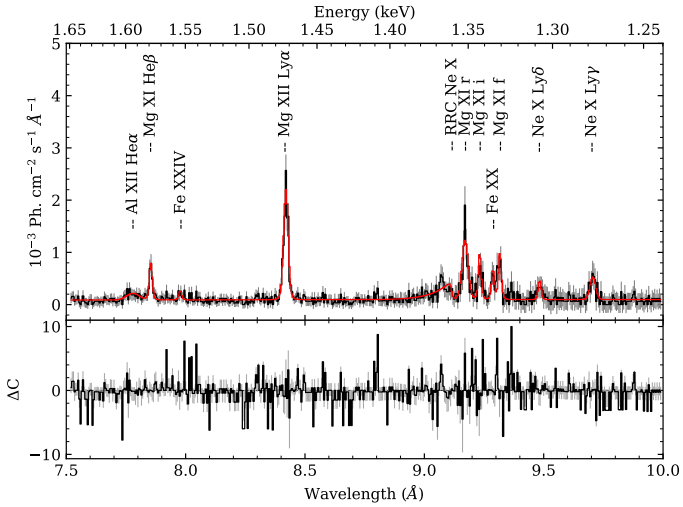

Fig. 7. Mg-region spectrum and best-fit model (red line), with residuals shown in the *bottom panel*.

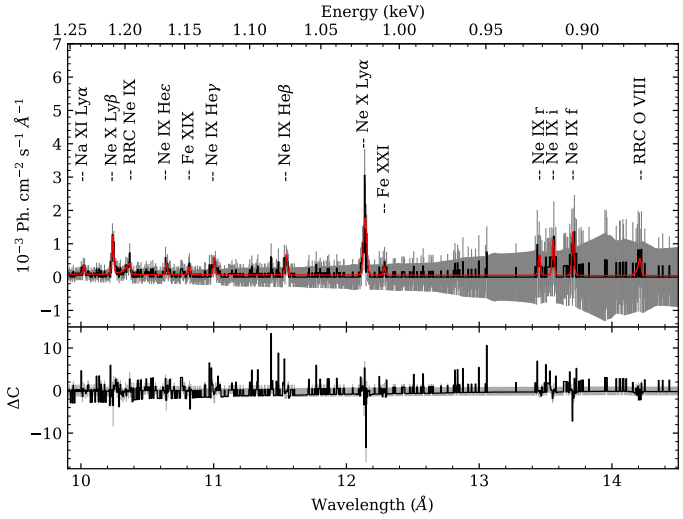

Fig. 8. Ne-region spectrum and best-fit model (red line), with residuals shown in the *bottom panel*.

codes require an input ionising continuum. We approximated such a continuum with a sum of two components, as previously done in Grinberg et al. (2017) and Lomaeva et al. (2020). The emission from the star, which dominates in the UV, was modelled with a black body, while the emission from the accretion onto the NS was modelled with a power law modified by a Fermi-Dirac cutoff. Both components have the same parameters as employed in Lomaeva et al. (2020). In particular, the shape of the power law continuum cannot be well constrained at energies below 10 keV, especially when strongly affected by absorption, as is the case with our observations. We thus used parameters derived from non-simultaneous *NuSTAR* observations (Fürst et al. 2014). We note that there are some indirect hints that the illuminating continuum assumed here may not reflect the true continuum seen by the plasma in the system, such as the large ratio between the Fe and Si/S fluorescence lines in particular and the stability curves, which are unstable over wide ranges, especially at the ionisation parameters of interest. This emphasises the importance of strictly simultaneous observations at high resolution below 10 keV and at energies above this range for the future.

In our modelling, we left the electron density $n_{\rm e}$ (cm^{-3}), the ionisation parameter ξ (erg cm s^{-1}), the absorption coefficient $N_{\rm H}$ (10^{22} cm^{-2}), and the turbulent velocity $v_{\rm turb}$ (km s^{-1}) free to vary. We explored the parameter space with CLOUDY in the ranges of $5.0 \leq \log n_{\rm e} \leq 11.5$, $0.0 \leq \log \xi \leq 4.0$, $20.9 \leq \log N_{\rm H} \leq 22.3$, and 80 km s^{-1} $\leq v_{\rm turb} \leq$160 km s^{-1}. For SPEX, we assume a much larger parameter space since its PION model calculates the ionisation balance instantaneously and does not require a predefined grid of models.

We modelled the data with an absorbed partially covered power law, with a spectral index of $\Gamma = 1$, corresponding to the input power law of our photoionisation models (Fürst et al. 2014), in addition to the CLOUDY/SPEX photoionisation model. The absorption due to the interstellar medium was fixed to 3.7×10^{21} cm^{-2} (HI4PI Collaboration 2016), while the local absorption was left free to vary. The local partial absorption was applied only to the continuum, since both the geometry of the system, with localised wakes of material, and previous high resolution studies (Schulz et al. 2002; Watanabe et al. 2006; Grinberg et al. 2017; Lomaeva et al. 2020) imply that the line producing region is not experiencing the same high absorption as the vicinity of the neutron star, where the continuum is produced. We further added three more Gaussians for the fluorescence Fe Kα line, centred at 1.9388 Å (cf. Sect. 4), and for the near-neutral fluorescence emission lines of S II-VIII and Si II-VI, which are not reproduced by CLOUDY or SPEX.

The best fit CLOUDY model resulted in $\log n_{\rm e} = 8.19984^{+0.00017}_{-0.01696}$, $\log \xi = 3.728 \pm 0.009$, with $\log N_{\rm H} = 22.175 \pm 0.020$ cm^{-2} and a turbulent velocity of ~160 km s^{-1}. The model required a redshift, with a best fit value of $z \sim 10^{-4}$, corresponding to a velocity of $v \sim 100$ km s^{-1}, which is consistent with the Doppler shifts previously obtained. The Cash (d.o.f.) statistic value was 1.58 (2584). The modelling of the whole spectrum with SPEX resulted in the best fit values of $\log \xi = 3.867^{+0.005}_{-0.009}$ and $N_{\rm H} = (4.3 \pm 0.3) \times 10^{21}$ cm^{-2}, with a line broadening of 160 ± 16 km s^{-1} and a Cash (d.o.f.) value of 1.57 (2382). Also in this case the model is redshifted with respect to the data, with a best fit velocity along the line of sight of 130^{+15}_{-20} km s^{-1}. Best fits are shown in Fig. 9.

We noticed that the electron density $n_{\rm e}$ is degenerate with the absorption of the interstellar medium (ISM): the larger the ISM $N_{\rm H}$, the larger the $n_{\rm e}$ (see discussion in Sect. 5.2). We also tried to add a second CLOUDY component, obtaining no statistical significant improvement of the fit.

5. Discussion

We performed, for the first time, a high-resolution spectroscopy analysis of *Chandra*/HETGS data of Vela X−1 at the orbital phase $\phi_{\rm orb} \approx 0.75$. At first glance, the hardness ratio (Fig. 2) revealed no significant continuum spectral variability during the observation. The mainly flat shape of the hardness ratio is not surprising, since the line of sight at this orbital phase is expected to lie well within the photoionisation wake, a denser stream-like region that trails the NS (Doroshenko et al. 2013; Malacaria et al. 2016) and acts as a constant absorber (see Fig. 1).

The analysis pointed out the presence of Fe, S, Si, Mg, and Ne, as well as of less intense emission lines from Al and Na. Contrary to previous observations (Schulz et al. 2002; Goldstein et al. 2004; Watanabe et al. 2006), there is no evidence of the presence of Ar ($\lambda \sim 3.359$ Å), Ca ($\lambda \sim 4.186$ Å), or Ni ($\lambda \sim 1.660$ Å) fluorescence lines. Upper limits of their fluxes

Table 6. Spectral features detected in the Mg region (10–14 Å).

Line	BB α	Ref. wavelength (Å)	Det. wavelength (Å)	Line flux (ph s^{-1} cm^{-2} $\times 10^{-5}$)	Velocity (km s^{-1})
Na XI Lyα[a]	2.5	10.023[b]	10.023 ± 0.005	$0.5^{+0.3}_{-0.2}$	0 ± 150
Ne X Lyβ	29	10.23887[c]	10.2408 ± 0.0017[d]	$2.1^{+0.6}_{-0.5}$	60 ± 50
Ne IX Heε[e]	3.2	10.643[b]	10.644 ± 0.006	$0.7^{+0.4}_{-0.3}$	30 ± 170
Fe XIX	1.8	10.816[b]	$10.814^{+0.006}_{-0.005}$	$0.4^{+0.3}_{-0.2}$	-60^{+170}_{-140}
Ne IX Heγ[f]	7	11.001[g]	$11.005^{+0.006}_{-0.007}$	$1.0^{+0.5}_{-0.4}$	110^{+160}_{-190}
Ne IX Heβ[h]	8	11.544[g]	$11.549^{+0.005}_{-0.006}$	$2.1^{+0.6}_{-0.5}$	130^{+130}_{-160}
Ne X Lyα	49	12.132[c]	12.1398 ± 0.0017	$5.3^{+1.2}_{-1.1}$ [i]	190 ± 40
Fe XXI	1.7	12.284[b]	$12.285^{+0.008}_{-0.007}$	$0.5^{+0.5}_{-0.4}$	20^{+200}_{-170}
Ne IX r	17	13.4476[j]	13.454 ± 0.005	$1.3^{+1.6}_{-0.7}$	140 ± 110
Ne IX i	17	13.553[j]	13.557 ± 0.005	$2.2^{+0.8}_{-0.6}$	$= v_{(\mathrm{Ne\,IX}\ r)}$
Ne IX f	17	13.699[j]	13.706 ± 0.005	$2.6^{+1.6}_{-1.3}$	$= v_{(\mathrm{Ne\,IX}\ r)}$

Notes. For each of them, we report the detection parameter α, the best-fit values (wavelength and line flux) and the Doppler velocities, computed with respect to the reference wavelength from the literature. Line widths were fixed to 0.003 Å if not stated otherwise. [a]Possible line blends include Fe XX at 10.024 Å and Ni XXIV at 10.027 Å. [b]Reference wavelength taken from AtomDB database (http://www.atomdb.org/index.php). [c]Erickson (1977). [d]Computed from the Ne X Lyα best fit wavelength, as from Erickson (1977). [e]Another possible identification is the Fe XIX at 10.648 Å. [f]Possible line blends are: Fe XX at 11.007 Å, Na X Heι at 11.003 Å, and Fe XIX at 11.002 Å. [g]Kelly (1987). [h]Another possible line is Fe XX at 11.546 Å. [i]Best-fit value of the line width of $\left(9.6^{+3.0}_{-2.8}\right) \times 10^{-3}$ Å. [j]Drake (1988).

Table 7. Best-fit values of the RRCs in each region, with a temperature reported in Kelvin and electronvolts.

RRC	Region	Threshold energy (keV)	Temperature (10^4 K)	Temperature (eV)	Wavelength (Å)
Mg XII	Si	1.961 ± 0.002	$5.2^{+6.7}_{-2.9}$	$4.5^{+5.8}_{-2.5}$	6.321
Mg XI	Si	1.768 ± 0.001	$3.6^{+1.9}_{-1.3}$	$3.1^{+1.6}_{-1.1}$	7.022
Ne X	Mg	$1.3600^{+0.0012}_{-0.0010}$	$12.5^{+3.9}_{-2.9}$	$10.8^{+3.4}_{-2.5}$	9.116
Ne IX	Ne	$1.1950^{+0.0006}_{-0.0007}$	$5.2^{+3.9}_{-2.4}$	$4.5^{+3.4}_{-2.1}$	10.374
O VIII	Ne	0.8720 ± 0.0006	$1.0^{+4.8}_{-0.7}$	$0.9^{+4.2}_{-0.6}$	14.218

Notes. The wavelengths in the last column are simply the conversion of the threshold energy from kiloelectronvolts to Ångström and are meant just for convenience to the reader.

Table 8. Best-fit values of the G and R ratios of the He-like triplets and correspondent electron temperatures and densities (Porquet & Dubau 2000).

Element	G	R	Temperature (K)	Temperature (eV)	Electron density n_e (cm^{-3})
S XV	$0.48^{0.14}_{-0.10}$	$9.9^{+2.4}_{-2.2}$	–	–	
Si XIII	$0.80^{+0.10}_{-0.09}$	6.0 ± 0.6	1×10^7	860	1×10^{12} (*)
Mg XI	$0.74^{+0.13}_{-0.14}$	$1.2^{+0.3}_{-0.2}$	7×10^6	600	2×10^{13}
Ne IX	$3.7^{+4.4}_{-1.7}$	$1.2^{+0.6}_{-0.5}$	$1 - 3 \times 10^6$	90–260	1.5×10^{12}

Notes. The electron density of the He-like Si XIII triplet (marked as (*)) is an upper limit.

resulted in 5.2×10^{-5} ph s^{-1} cm^{-2} for Ar, 2.3×10^{-5} ph s^{-1} cm^{-2} for Ca, and 3.1×10^{-4} ph s^{-1} cm^{-2} for Ni, respectively. In the next subsections, we discuss the Fe region in detail (Sect. 5.1), carry out a plasma diagnostic (Sect. 5.2), and investigate the geometry of the wind of the companion star (Sect. 5.3).

5.1. The Iron complex

The Fe region (1.6–2.5 Å) is dominated by a Fe Kα line, centred at 1.9388 ± 0.0006 Å. Assuming no Doppler shift for the line, the corresponding maximum ionisation state is Fe X (Palmeri et al. 2003), which is consistent with the results of Grinberg et al. (2017) (below Fe XII), and different from the case of an irradiated wind, as shown by the hydrodynamic simulations of Sander et al. (2018) (where the wind is mainly driven by Fe III ions). However, the line may be redshifted so that a higher ionisation state could be expected. A more refined calculation is beyond the scope of this paper. The only other relevant feature detected in this region is the Fe K-edge at 1.742 ± 0.003 Å (see Table 2), which is not significantly Doppler shifted.

The BB algorithm did not detect the Fe Kβ line expected at ∼1.758 Å, most likely because of the proximity of the Fe

K-edge. However, since the average flux ratio between the Fe Kβ and Fe Kα lines is 0.13–0.14 (Palmeri et al. 2003, for the charge states Fe II-IX), we can estimate an expected flux of $(1.32 \pm 0.11) \times 10^{-4}$ ph cm^{-2} s^{-1}, which might not be sufficient to let the line emerge from the continuum underneath. To verify this assertion, we generated 1000 Monte Carlo simulated spectra adding a Gaussian to the best fit model at the correspondent wavelength of the Fe Kβ with the expected flux. We then ran the BB algorithm on all the simulated spectra (cf. Sect. 3.1). In no case was the line detected, confirming its weakness with respect to the X-ray continuum and the K-edge, which precluded a detection in the observational data. The Fe Kβ/Kα ratio depends on the ionisation of iron (see the detailed discussions in Molendi et al. 2003; Bianchi et al. 2005). For higher charge states, the expected line ratio is even smaller, that is, the Fe Kβ line would be even weaker than what our simulation showed as undetectable. Therefore, we cannot rule out that the ionisation state is higher than what we assumed. We discuss the prospects of detecting Fe Kβ with future instruments in Sect. 6.

Results from Goldstein et al. (2004) at $\phi_{\rm orb} \approx 0$ and $\phi_{\rm orb} \approx 0.5$ show, in the same spectral region, the presence of the Ni Lyα line at $\lambda \sim 1.660$ Å, while Schulz et al. (2002) proposed the presence of a Fe XXV emission line at $\lambda \sim 1.85$ Å ($\phi_{\rm orb} \approx 0$). The BB procedure did not detect any features at those wavelengths, but after a visual inspection, we noted a marginal presence of residuals in emission. So we added two more Gaussians to the best fit model of the Fe region at $\lambda \sim 1.66$ Å and $\lambda \sim 1.86$ Å for the Ni Lyα and a Fe XXV, respectively, and fitted the spectrum again. The Fe XXV is actually a He-like triplet, but the resolution of the MEG of 0.023 Å FWHM, adopted consistently through the paper, is not good enough to resolve the lines individually. Hence, we used just one Gaussian to fit the whole ion, letting the width free to vary. The width of the Ni Lyα line was fixed to the usual value of 0.003 Å. The fluxes of these latter Gaussians resulted in $\left(1.8^{+1.3}_{-1.2}\right) \times 10^{-4}$ ph cm^{-2} s^{-1} for the Ni Lyα and $(3.1 \pm 1.2) \times 10^{-4}$ ph cm^{-2} s^{-1} for the Fe XXV lines, while the width of the He-like Fe XXV had a best fit value of $0.018^{+0.013}_{-0.007}$ Å.

From the Fe edge (Table 2), we computed the equivalent hydrogen column as $N_{\rm H} = \tau_{\rm edge}/(Z_{\rm Fe}\sigma_{\rm Fe})$, where $Z_{\rm Fe} = 2.69 \times 10^{-5}$ is the solar Fe abundance (Wilms et al. 2000) and $\sigma_{\rm Fe} = 3.4 \times 10^{-20}$ cm^2 is the photoelectric absorption cross section for Fe XXV at the wavelength of the K-edge (Verner et al. 1996). Using the best-fit value optical depth $\tau_{\rm edge} = 0.31 \pm 0.03$, we derived $N_{\rm H} = (3.4 \pm 0.3) \times 10^{23}$ cm^{-2}, which is nearly consistent with the best-fit value of $N_{\rm H} = (2.68 \pm 0.07) \times 10^{23}$ cm^{-2} obtained fitting the spectrum in this region with a simple absorbed power law, with solar abundances and cross sections as specified in Sect. 3. These values are of the same order of magnitude as the best fit values found for observations using MAXI (Matsuoka et al. 2009) by Doroshenko et al. (2013) and *NuSTAR* (Harrison et al. 2013) by Fürst et al. (2014) at the same orbital period. However, we must bear in mind here that the model we used does not account for the Fe Kβ line, which may contribute to larger uncertainties on the Fe K-edge parameters.

5.2. Plasma properties

The presence of five narrow RRCs (Mg XI, Mg XII, Ne IX, Ne X, and O VIII) suggests that the plasma is photoionised, with a temperature between ∼1 and 10 eV (Table 7). A further indication of a photoionised plasma might be the value of $G = 3.7^{+4.4}_{-1.7}$ of the Ne IX triplet (Table 8), which is consistent with four in spite of the large uncertainties (Porquet & Dubau 2000).

However, the G ratios of S XV ($G = 0.48^{+0.14}_{-0.10}$), Si XIII ($G = 0.80^{+0.10}_{-0.09}$), and Mg XI ($G = 0.74^{+0.13}_{-0.14}$) are all smaller than one, indicating that collisional processes are not negligible and may even dominate (Porquet & Dubau 2000; Porquet et al. 2010). Under the hypothesis of a collisional equilibrium plasma (CIE), we can estimate the temperature from the G ratio values (Porquet & Dubau 2000). From the He-like Si XIII and Mg XI triplets, we obtain temperatures of $\sim 1 \times 10^7$ K and $\sim 7 \times 10^6$ K, respectively, which are two orders of magnitude higher than the ones from the Ne RRCs.

This inconsistency between temperatures derived from the RRCs and the He-like line ratios is likely due to the known issue that relative level populations between the upper levels of the He-like triplet lines can be shifted by other physical phenomena, which are likely present in HMXBs, thus making the G ratio unreliable. In particular, two processes can enhance a resonant r line stronger than the intercombination i or forbidden f lines: photoexcitation and resonance line scatter. Photoexcitation can be important in photoionisation equilibrium (PIE) plasma, when many photons with the right energy excite the electrons to the resonant level. This clearly enhances the resonance line and, then, alters the G ratio with respect to the pure recombination case (see the comprehensive explanation in Kinkhabwala et al. 2002). The presence of a few weak iron L emission lines (Fe XIX-XXIV) also seems to point in this direction (Sako et al. 2000).

Resonant line scattering occurs when a photon is absorbed and re-emitted in the same wavelength, but in the direction of the lowest optical depth. This phenomenon is well explained by Wojdowski et al. (2003) for the HMXB Centaurus X-3, observed during eclipse. In the case of Vela X−1, though we are not in the eclipsing phase, the dense streams of matter surrounding the NS can act as a strong absorber, enhancing the resonance line scattering into the line of sight.

Concerning the R ratio, the values of Mg XI ($R = 1.2^{+0.3}_{-0.2}$) and Ne IX ($R = 1.2^{+0.6}_{-0.5}$) He-like lines imply an electron density of the plasma of $\sim 2 \times 10^{13}$ cm^{-3} and $\sim 1.5 \times 10^{12}$ cm^{-3}, respectively, considering a plasma temperature of 7×10^6 K and 2×10^6 K, as previously estimated[5]. On the other hand, the R ratios of Si XIII ($R = 6.0 \pm 0.6$) and S XV ($R = 9.9^{+2.4}_{-2.2}$) are much higher than the respective values at the low density limit, when the relative intensities of the He-like lines are in fact independent of the electron density of the plasma. In the case of Si, for instance, the low density limit value is $R = 3$, corresponding to a maximum density of the order of 10^{12} cm^{-3} (Porquet & Dubau 2000), which can be addressed here as an upper limit. On the other hand, the fit with CLOUDY and SPEX photoionisation models highlighted the degeneracy of the electron density $n_{\rm e}$ with the model chosen for the continuum, and, in particular, with the absorption from the ISM. The best fit value of $n_{\rm e} = 1.5 \times 10^8$ cm^{-3}, for instance, can be treated only as a lower limit. The analysis underlines that the estimation of the density is influenced in opposite directions by the R ratio and the continuum and the real value is somewhere in between those limits.

Also the UV radiation of the companion star can alter the plasma (the so-called UV-pumping mechanism, Gabriel & Jordan 1969; Blumenthal et al. 1972; Mewe & Schrijver 1978; Porquet et al. 2001). UV radiation mimics a high density plasma, favouring the population of the ^3P levels against the $^3S_1$ level,

[5] We note here that the R ratio depends upon the relative ionic abundance of the H-like and He-like ions ($\chi_{\rm ion}$ parameter), but in the range of our interest the dependence is so small that we can neglect it (see Fig. 9 of Porquet & Dubau 2000).

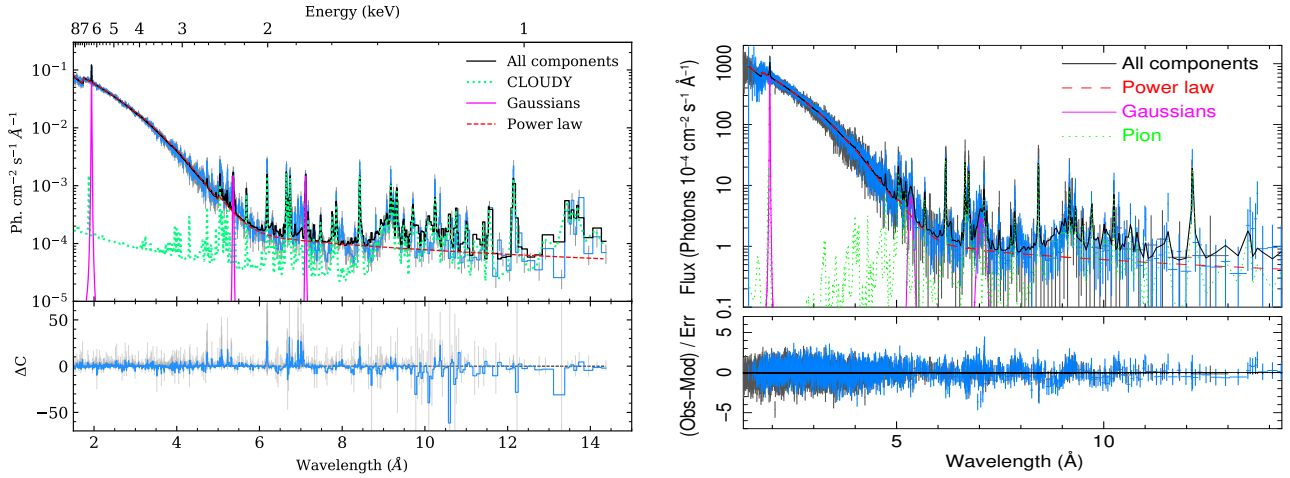

Fig. 9. Fit of the whole spectrum with the photoionisation model (dotted green line) from CLOUDY (*left panel*) and SPEX (*right panel*), plus a partially covered power law (dotted red line), and three Gaussians for the fluorescence lines of Fe Kα, S II-VIII, and Si II-VI (solid magenta lines). The total fit function is represented in black. The residuals of fit are in the bottom panels. Spectra were re-binned for the sake of clarity.

leading to an increase in the intensity of the intercombination line, against the forbidden line, and, hence, to smaller values of the R ratio. The influence of the UV emission is taken into account in both CLOUDY- and SPEX-based photoionisation models, through our choice of the continuum. Such models should also, if applicable to the given data at all, give better constrains on the underlying plasma parameters than the more empirical consideration of G and R ratios. The quality of our fits in Sect. 4 implies that this is the case.

Overall, both the self-consistent photoionisation codes provided a satisfactory fit of the data (Fig. 9), implying that, at this specific orbital phase, the plasma is mainly photoionised. However, a closer inspection at the residuals hints to the presence of at least another phase of the plasma. The near-neutral emission lines of S II-VIII and Si II-VI, as well as the Fe Kα line, are not reproduce by the photoionisation models that are driven by the presence of highly ionised lines. This naturally suggests that the plasma cannot be a single component plasma.

In a possible scenario, colder and denser clumps of plasma, from either the wind or larger scale accretion structures such as wakes, can cross the line of sight unevenly, adding a further component with a lower ionisation to the PIE emission of the wind of the companion star. Our data do not allow one to constrain the origin of this component that could be, for example, a further, colder PIE component, a collisionally ionised component, or a more complex mix with a temperature gradient as is the case, for example, in Cyg X−1 (Hirsch et al. 2019). We also note that our results emphasise the necessity of an accurate treatment of intermediate and low ionisation ions in atomic codes used for high resolution X-ray spectroscopy.

5.3. Wind geometry

Doppler velocities at different orbital phases can reveal the location and the dynamics of line emitting material. Figure 10 shows the velocities for the ions of Si VI-IX from Schulz et al. (2002) and Goldstein et al. (2004) at the orbital phases $\phi_{\rm orb} \approx 0$ and $\phi_{\rm orb} \approx 0.5$, adjusted with respect to the laboratory measurements of Hell et al. (2016), together with the ones from Grinberg et al. (2017) at the orbital phase of $\phi_{\rm orb} \approx 0.25$, and with those in the present work ($\phi_{\rm orb} \approx 0.75$). Velocities at $\phi_{\rm orb} \approx 0.25$ are negative (blueshift), while velocities at the other orbital phases are positive (redshift) and/or consistent with no shift. The same

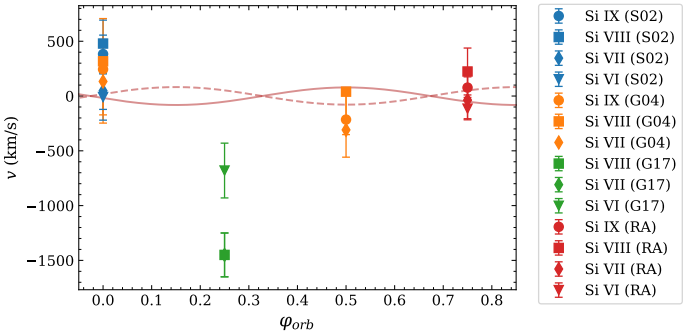

Fig. 10. Doppler velocities at different orbital phases of Si IX (circles), Si VIII (squares), Si VII (diamonds), and Si VI (upside down triangles), from Schulz et al. (2002, S02, blue) and Goldstein et al. (2004, G04, orange), as adjusted for laboratory reference values by Hell et al. (2016), from Grinberg et al. (2017, G17, green), and from the present work (RA, red). The solid and dashed lines stand for the radial velocities of the NS and the giant star, respectively.

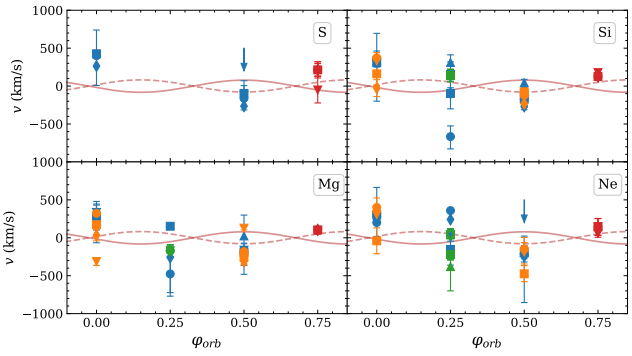

Fig. 11. Doppler velocities at different orbital phases of Lyα lines and He-like triplets of S, Si, Mg, and Ne from Schulz et al. (2002) (blue) and Goldstein et al. (2004) (orange), from Grinberg et al. (2017) (green), and from the present work (red). Different symbols stand for different ionisation stages. The solid and dashed lines represent the radial velocities of the NS and of the companion star, respectively.

behaviour is also observed for all the other lines of S, Si, Mg, and Ne (Fig. 11), even though there are no recent laboratory measurements that allow us to validate the Doppler shifts found by

the previous studies (Schulz et al. 2002; Watanabe et al. 2006; Goldstein et al. 2004; Grinberg et al. 2017). Most of the velocities are consistent with the radial velocity of the NS, as well as of the companion star (solid and dashed lines in Figs. 10 and 11), computed as follows:

$$v_{\rm rad} = \frac{2\pi a}{T\sqrt{1-e^2}} \sin i[\cos(\vartheta+\omega) + e\cos\omega], \quad (1)$$

where a is the semi-major axis, i is the inclination, T is the orbital period, e is the eccentricity, and ϑ and ω are the true anomaly and the argument of periapsis, respectively.

The overall behaviour is consistent with the material comoving with the NS, though the lack of more observational data for each orbital phase prevents us from asserting this definitively. However, this behaviour has already been observed for the black hole HMXB Cygnus X−1 (Hirsch et al. 2019; Miškovičová et al. 2016), where the Doppler shifts show a clear modulation with the orbital phase. It has already been suggested for Vela X−1 that the wind velocity at the distance of the NS is $\sim$100 km s^{-1} and lower than typically estimated from prescribed simple β-laws (Sander et al. 2018). The large spread in the range of observed Doppler shifts within the same orbital phases may be due to radiation coming from regions further downstream the wind or due to a more complex velocity structure in the accretion region.

More considerations on the geometry of the emitting region can be drawn from the ionisation state of the plasma. The ionisation parameter can be expressed as in Tarter et al. (1969):

$$\xi = \frac{L_X}{n_{\rm e} r^2}, \quad (2)$$

where L_X is the X-ray luminosity of the source, $n_{\rm e}$ is the particle density of the plasma, and r is the distance at which the lines are produced. From the photoionisation models, we computed the distributions of the relative abundances of all the ions as a function of ξ. For the H-like ions, the ionisation parameter was in the range of $3.7 \geq \log(\xi) \geq 4.2$. Assuming that each ion is produced at the peak of its distribution, for a luminosity of 4×10^{36} erg s^{-1} and a best-fit value of $\log(n_{\rm e}) \sim 8$, we obtained a distance in the range of $(1.6–2.8) \times 10^{12}$ cm = 23–40 $R_\odot$. Considering that the orbital separation of the system is $\sim$50 $R_\odot$ and the companion star has a radius of about 30 $R_\odot$, the region where the H-like emission lines come from seems to be very close to the surface of the companion star, rather than to the surface of the NS. The other ionisation stages have lower values of $\log(\xi)$, implying even higher distances, compatible with the idea of a wake expanding after the passage of the NS. We note, however, that this estimate assumes a constant density, which is most likely not the case for an expanding wind, even without taking possible clumping and wake structures into account.

Our result is in agreement with simulations of X-ray photons in a smooth wind from Watanabe et al. (2006) for H-like Si in the case of a mass loss rate of $\dot{M} \leq 1.0 \times 10^{-6}\, M_\odot\, {\rm yr}^{-1}$, which is consistent with the latest estimation for Vela X−1 of $\sim 0.7 \times 10^{-6}\, M_\odot\, {\rm yr}^{-1}$ (Sander et al. 2018). In the end, our simple calculation would suggest that the photoionised plasma is produced at the orbital separation of the system in a region close to the surface of the companion star.

Nonetheless, given the uncertainty of the electron density driven by the continuum, we repeated the calculation using the $n_{\rm e}$ derived from the R ratio instead ($n_{\rm e} \sim 10^{12}$ cm^{-3}). This n_e value, however, does not take the presence of the strong UV radiation from the stellar wind into account (Sect. 5.2) and thus has to be considered as an overestimate. For the same values of the ionisation parameter as before, the resulting distance is $r \lesssim 0.5\, R_\odot$, which is comparable with the Bondi-Hoyle-Littleton radius of the NS in Vela X−1 of $\sim 10^{10}$ cm (Manousakis & Walter 2015). The assumption of using the same ionisation parameters holds because $\log(\xi)$ is primarily driven by the ionisation state and thus hardly changes with the electron density, which is instead driven by the absolute line strength (i.e., distance and continuum) and the triplet shape if the lines are well resolved. In this case, of course, the ionisation of the wind would be due almost entirely to the gravitational pulling of the NS. From this analysis, we cannot infer the presence of clumps.

6. Future perspectives with XRISM/Resolve and *Athena*/X-IFU

High-resolution spectroscopy is a powerful tool to study X-ray emission from any kind of astrophysical plasma. Currently, limitations of X-ray satellites are due, for instance, to their intrinsic resolution and sensibility. New generation X-ray satellites will go beyond these limits. The X-Ray Imaging and Spectroscopy Mission (XRISM, formerly XARM, Tashiro et al. 2018) and the Advanced Telescope for High Energy Astrophysics (*Athena*, Nandra et al. 2013) will host on-board microcalorimeters with an energy resolution down to a few electronvolts, thus exceeding the resolution of *Chandra* gratings in the Fe K region.

We performed simulations of this region (1.6–2.2 Å, cf. Sect. 5.1), including the Fe K-edge and the Fe Kα as detected in the *Chandra* observation, and the Fe Kβ, the He-like Fe XXV, and the Ni Kα with the upper limit on the flux as in Sect. 5.1. Both microcalorimeters should be able to resolve the Fe Kα doublet and the Fe XXV triplet. To assess this in more detail, the input spectrum of our simulation included two Gaussians for the Fe Kα at 1.9399 Å for the Fe Kα_1 and at 1.9357 Å for Fe Kα_2, respectively, with a 1:2 ratio (Kaastra & Mewe 1993), and four Gaussians for the Fe XXV, with line centroids as in Drake (1988) and a flux ratio of 2:1:1:2 (w:x:y:z). The width of all the lines was fixed to 0.0007 Å (~2 eV).

XRISM will be provided with the soft X-ray spectrometer Resolve, with a nominal energy resolution of 5–7 eV in the 0.3–12 keV bandpass. We used the ancillary and response files of Hitomi/SXS (Kelley et al. 2016) for the energy resolution requirement of 7 eV. Simulations show that an exposure of only 300 s (comparable with the pulse period of 293 s) is sufficient to clearly detect the Fe Kβ line with a significance of $\alpha = 1.8$, corresponding to 83% of positive detection probability, with a measured Fe Kβ/Kα ratio of $0.17^{+0.11}_{-0.09}$. With an exposure of 2.5 ks, the probability of a positive detection of the Fe Kβ line raises up to >99.99% ($\alpha = 22$). The Fe Kα doublet is resolved, while amongst the lines of Fe XXV, only the f line is clearly resolved.

Athena will be equipped with the X-ray Integral Field Unit (X-IFU, Barret et al. 2018), a cryogenic X-ray spectrometer working in the energy range of 0.2–12 keV, with a nominal energy resolution of 2.5 eV up to 7 keV. Moreover, thanks to the higher collecting area of *Athena* (1.4 m^2 at 1 keV), high quality spectra will be acquired in much shorter exposures. Also for the *Athena*/X-IFU, we performed a 300 s simulation of the Fe region (Fig. 12). Running the BB algorithm on the simulated spectrum, the Kβ line is detected with $\alpha = 9$, corresponding to 99.99% probability of positive detection. If the exposure times is increased up to 2.5 ks, then the Kβ line is detected with a significance of $\alpha = 69$. The measured intensity ratio between the Fe Kβ and Fe Kα is $0.16^{+0.10}_{-0.08}$. The Fe Kα doublet is fully resolved, as well as the f line of Fe XXV. The i line, which consists of two

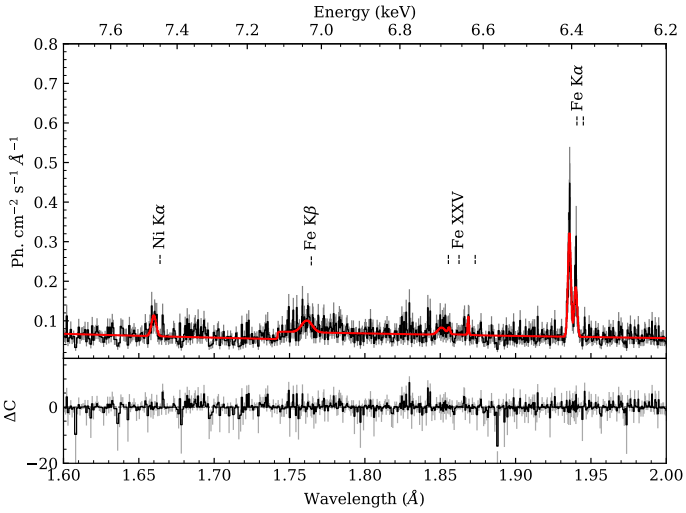

Fig. 12. Simulated spectrum of the Fe region with the *Athena*/X-IFU and best fit model, with residuals in the *lower panel*. Exposure time of 300 s, data binned with a minimum of 15 counts/bin.

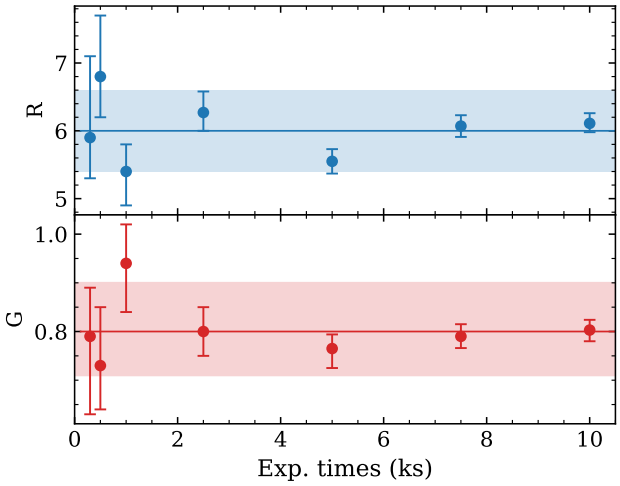

Fig. 13. *R* and *G* ratios for the He-like triplet of Si as obtained from simulations with *Athena*/X-IFU with different exposure times. Solid lines correspond to the best fit values with the error ranges given by the coloured areas obtained from the present work.

lines ($(x + y)$ in the nomenclature of Gabriel 1972), is partially resolved, with the most energetic one blended with the *r* line.

Athena's capabilities will significantly also improve the plasma diagnostic, even at shorter exposures. To test how well we can determine *R* and *G* ratios, we performed simulations with *Athena*/X-IFU at different exposure times. Figure 13 shows the ratios of the Si regions at different exposures, in comparison with the ratios obtained from the analysis of the 45.88 ks *Chandra*/HETGS observational data set. With an exposure of only 2.5 ks, the uncertainties on *R* and *G* are reduced to ∼50%. Longer exposures consistently reduce the errors on *R* and *G*, from ∼10% up to 2% of their absolute values.

All the discussed simulations with *Athena*/X-IFU were performed using standard response matrices and background files[6]. A more thorough exploration of possibilities to observe Vela X−1 with *Athena*, including a detailed modelling of the effects of defocussing necessary to avoid pile-up for bright X-ray binaries and the right choice of event grades to address certain scientific questions, is beyond the scope of this work and will be addressed in a dedicated publication.

Overall, the achievement of good-quality spectra with such short exposure times implies that the lines can be traced on shorter timescales, of the same order of magnitude as the pulsar period. Moreover, because of *Athena*'s resolution, the energy of the Fe Kα line can be better constrained so that we can be able to determine the ionisation stage of iron with a higher precision. It is clear, then, that upcoming X-ray satellites will considerably improve the knowledge of HMXBs, of stellar winds, and, in general, of any kind of astrophysical plasma, as well remarked by XRISM Science Team (2020).

7. Conclusions

We conducted, for the first time, X-ray high-resolution spectroscopy of Vela X−1 at the orbital phase $\phi_{\rm orb} \approx 0.75$, when the line of sight is going through the photoionisation wake that trails the neutron star along the orbit. The data did not show any significant variability of the continuum for the duration of the observation. A blind search for spectral features lead us to detect emission lines from Fe, S, Si, Mg, and Ne, and, to a lesser degree, from Al and Na. We detected and identified five narrows RRCs (Mg XI-XII, Ne IX-X, O VIII) and He-like triplets of S, Si, Mg, and Ne.

From plasma diagnostic techniques and from fits with photoionisation models from CLOUDY and SPEX, we conclude that the plasma at this orbital phase is mainly photoionised, but data suggest the presence of at least another component, with a smaller ionisation parameter. The presence of a collisional component cannot be excluded, as well as a mixture of ionised and collisional phases. This is in agreement with the idea of colder and denser clumps of matter, embedded in the hot, optically-thin wind of the donor star. The complex geometry of the system is also reflected by the spread of the distribution of the Doppler velocities, as well as in the indetermination of the emission region.

The future X-ray instruments *Athena*/X-IFU and XRISM/Resolve will considerably enhance the detection and the resolution of spectral features. We show through simulations that, thanks to higher energy resolutions, they will resolve single lines in the Fe Kα doublets and Fe XXV triplet and, thanks to higher collecting areas, will allow plasma diagnostic[7] for time scales as short[8] as a few hundreds of seconds.

Acknowledgements. Authors acknowledge financial contribution from the agreement ASI-INAF n.2017-14-H.0, from INAF mainstream (PI: T. Belloni). V.G. is supported through the Margarete von Wrangell fellowship by the ESF and the Ministry of Science, Research and the Arts Baden-Württemberg. S.B. acknowledges financial support from the Italian Space Agency under grant ASI-INAF 2017-14-H.O. Work at LLNL was performed under the auspices of the US Department of Energy under contract No. DE-AC52-07NA27344 and supported through NASA grants to LLNL. This research has made use of NASA's Astrophysics Data System Bibliographic Service (ADS) and of ISIS functions (`isisscripts`) provided by ECAP/Remeis observatory and MIT. For the initial data exploration, this research used the *Chandra* Transmission Grating Data Catalog and Archive (`tgcat`; Huenemoerder et al. 2011). This research also has used the following `nPython` packages: `nMatplotlib` (Hunter 2007), `nNumpy` (Oliphant 2006), `nPandas` (McKinney 2010), and the community-developed

[6] Response matrices for the *Athena*/X-IFU can be found at: `http://x-ifu-resources.irap.omp.eu/PUBLIC/RESPONSES/CC_CONFIGURATION/`. Background files are available at: `http://x-ifu-resources.irap.omp.eu/PUBLIC/BACKGROUND/CC_CONFIGURATION/`

[7] `http://www.sternwarte.uni-erlangen.de/isis/`

[8] `http://tgcat.mit.edu/`

`Astropy` (Astropy Collaboration 2018). We in particular thank M. Nowak for the implementation of the Bayesian block algorithm used in this work, M. Guainazzi for his input on XRISM simulations, and I. El Mellah for helpful discussions.

References

Arnaud, K. A. 1996, in Astronomical Data Analysis Software and Systems V, eds. G. H. Jacoby, & J. Barnes, ASP Conf. Ser., 101, 17
Astropy Collaboration (Price-Whelan, A. M., et al.) 2018, AJ, 156, 123
Barret, D., Lam Trong, T., den Herder, J. W., et al. 2018, in Proc. SPIE, SPIE Conf. Ser., 10699, 106991G
Bearden, J. A., & Burr, A. F. 1967, Rev. Mod. Phys., 39, 125
Bianchi, S., Miniutti, G., Fabian, A. C., & Iwasawa, K. 2005, MNRAS, 360, 380
Blondin, J. M., Kallman, T. R., Fryxell, B. A., & Taam, R. E. 1990, ApJ, 356, 591
Blumenthal, G. R., Drake, G. W. F., & Tucker, W. H. 1972, ApJ, 172, 205
Brown, G. V., Beiersdorfer, P., Liedahl, D. A., Widmann, K., & Kahn, S. M. 1998, ApJ, 502, 1015
Canizares, C. R., Davis, J. E., Dewey, D., et al. 2005, PASP, 117, 1144
Cash, W. 1979, ApJ, 228, 939
Chakraborty, P., Ferland, G. J., Bianchi, S., & Chatzikos, M. 2020, Res. Notes Am. Astron. Soc., 4, 184
Doroshenko, V., Santangelo, A., Nakahira, S., et al. 2013, A&A, 554, A37
Drake, G. W. 1988, Can. J. Phys., 66, 586
El Mellah, I., Sundqvist, J. O., & Keppens, R. 2018, MNRAS, 475, 3240
El Mellah, I., Sander, A. A. C., Sundqvist, J. O., & Keppens, R. 2019, A&A, 622, A189
Erickson, G. W. 1977, J. Phys. Chem. Ref. Data, 6, 831
Ferland, G. J., Chatzikos, M., Guzmán, F., et al. 2017, RM&AC, 53, 385
Forman, W., Jones, C., Tananbaum, H., et al. 1973, ApJ, 182, L103
Foster, A. R., Ji, L., Smith, R. K., & Brickhouse, N. S. 2012, ApJ, 756, 128
Foster, A. R., Smith, R. K., & Brickhouse, N. S. 2017, in Atomic Processes in Plasmas (APiP 2016), Am. Inst. Phys. Conf. Ser., 1811, 190005
Fürst, F., Kreykenbohm, I., Pottschmidt, K., et al. 2010, A&A, 519, A37
Fürst, F., Pottschmidt, K., Wilms, J., et al. 2014, ApJ, 780, 133
Gabriel, A. H. 1972, MNRAS, 160, 99
Gabriel, A. H., & Jordan, C. 1969, MNRAS, 145, 241
Garcia, J. D., & Mack, J. E. 1965, J. Opt. Soc. Am. (1917-1983), 55, 654
Giménez-García, A., Shenar, T., Torrejón, J. M., et al. 2016, A&A, 591, A26
Goldstein, G., Huenemoerder, D. P., & Blank, D. 2004, AJ, 127, 2310
Grinberg, V., Hell, N., El Mellah, I., et al. 2017, A&A, 608, A143
Haberl, F., & White, N. E. 1990, ApJ, 361, 225
Harrison, F. A., Craig, W. W., Christensen, F. E., et al. 2013, ApJ, 770, 103
Hell, N., Brown, G. V., Wilms, J., et al. 2016, ApJ, 830, 26
HI4PI Collaboration (Ben Bekhti, N., et al.) 2016, A&A, 594, A116
Hiltner, W. A., Werner, J., & Osmer, P. 1972, ApJ, 175, L19
Hirsch, M., Hell, N., Grinberg, V., et al. 2019, A&A, 626, A64
Huenemoerder, D. P., Mitschang, A., Dewey, D., et al. 2011, AJ, 141, 129
Hunter, J. D. 2007, Comput. Sci. Eng., 9, 90
Joss, P. C., & Rappaport, S. A. 1984, ARA&A, 22, 537
Kaastra, J. S., & Mewe, R. 1993, A&AS, 97, 443
Kaastra, J. S., & Mewe, R. 1995, A&A, 302, L13
Kaastra, J. S., Mewe, R., & Nieuwenhuijzen, H. 1996, in UV and X-ray Spectroscopy of Astrophysical and Laboratory Plasmas, eds. K. Yamashita, & T. Watanabe, 411
Kaastra, J. S., Raassen, A. J. J., de Plaa, J., & Gu, L. 2018, `https://doi.org/10.5281/zenodo.2419563`
Kaper, L., Hammerschlag-Hensberge, G., & Zuiderwijk, E. J. 1994, A&A, 289, 846
Kelley, R. L., Akamatsu, H., Azzarello, P., et al. 2016, in The Astro-H high Resolution Soft X-ray sSpectrometer, SPIE Conf. Ser., 9905, 99050V
Kelly, R. L. 1987, J. Phys. Chem. Ref. Data, 17
Kinkhabwala, A., Sako, M., Behar, E., et al. 2002, ApJ, 575, 732
Kreykenbohm, I., Wilms, J., Kretschmar, P., et al. 2008, A&A, 492, 511
Liao, Z., Liu, J., Zheng, X., & Gou, L. 2020, MNRAS, 492, 5922
Lodders, K., Palme, H., & Gail, H. P. 2009, Landolt Börnstein, 4B, 712
Lomaeva, M., Grinberg, V., Guainazzi, M., et al. 2020, A&A, 641, A144
Malacaria, C., Mihara, T., Santangelo, A., et al. 2016, A&A, 588, A100
Manousakis, A. 2011, Dissertation, Université de Genève, Switzerland
Manousakis, A., & Walter, R. 2015, A&A, 575, A58
Martínez-Núñez, S., Torrejón, J. M., Kühnel, M., et al. 2014, A&A, 563, A70
Matsuoka, M., Kawasaki, K., Ueno, S., et al. 2009, PASJ, 61, 999
McClintock, J. E., Rappaport, S., Joss, P. C., et al. 1976, ApJ, 206, L99
McKinney, W., et al. 2010, Proceedings of the 9th Python in Science Conference, 445, 51, Austin, TX
Mewe, R., & Schrijver, J. 1978, A&A, 65, 99
Miškovičová, I., Hell, N., Hanke, M., et al. 2016, A&A, 590, A114
Molendi, S., Bianchi, S., & Matt, G. 2003, MNRAS, 343, L1
Nandra, K., Barret, D., Barcons, X., et al. 2013, ArXiv e-prints [arXiv:`1306.2307`]
Noble, M. S., & Nowak, M. A. 2008, PASP, 120, 821
Odaka, H., Khangulyan, D., Tanaka, Y. T., et al. 2013, ApJ, 767, 70
Oliphant, T. E. 2006, A guide to NumPy, 1 (USA: Trelgol Publishing)
Palmeri, P., Mendoza, C., Kallman, T. R., Bautista, M. A., & Meléndez, M. 2003, A&A, 410, 359
Porquet, D., & Dubau, J. 2000, A&AS, 143, 495
Porquet, D., Mewe, R., Dubau, J., Raassen, A. J. J., & Kaastra, J. S. 2001, A&A, 376, 1113
Porquet, D., Dubau, J., & Grosso, N. 2010, Space Sci. Rev., 157, 103
Quaintrell, H., Norton, A. J., Ash, T. D. C., et al. 2003, A&A, 401, 313
Sako, M., Liedahl, D. A., Kahn, S. M., & Paerels, F. 1999, ApJ, 525, 921
Sako, M., Kahn, S. M., Paerels, F., & Liedahl, D. A. 2000, ApJ, 543, L115
Sander, A. A. C., Fürst, F., Kretschmar, P., et al. 2018, A&A, 610, A60
Scargle, J. D., Norris, J. P., Jackson, B., & Chiang, J. 2013, ApJ, 764, 167
Schulz, N. S., Canizares, C. R., Lee, J. C., & Sako, M. 2002, ApJ, 564, L21
Tarter, C. B., Tucker, W. H., & Salpeter, E. E. 1969, ApJ, 156, 943
Tashiro, M., Maejima, H., Toda, K., et al. 2018, in Proc. SPIE, SPIE Conf. Ser., 10699, 1069922
Tzanavaris, P., & Yaqoob, T. 2018, ApJ, 855, 25
van den Eijnden, J., Degenaar, N., Schulz, N. S., et al. 2019, MNRAS, 487, 4355
van Loon, J. T., Kaper, L., & Hammerschlag-Hensberge, G. 2001, A&A, 375, 498
Verner, D. A., Ferland, G. J., Korista, K. T., & Yakovlev, D. G. 1996, ApJ, 465, 487
Wargelin, B. J., Beiersdorfer, P., Liedahl, D. A., Kahn, S. M., & von Goeler, S. 1998, ApJ, 496, 1031
Watanabe, S., Sako, M., Ishida, M., et al. 2006, ApJ, 651, 421
Weisskopf, M. C., Tananbaum, H. D., Van Speybroeck, L. P., & O'Dell, S. L. 2000, in Proc. SPIE, eds. J. E. Truemper, & B. Aschenbach , SPIE Conf. Ser., 4012, 2
Wilms, J., Allen, A., & McCray, R. 2000, ApJ, 542, 914
Wojdowski, P. S., Liedahl, D. A., Sako, M., Kahn, S. M., & Paerels, F. 2003, ApJ, 582, 959
XRISM Science Team 2020, Science with the X-ray Imaging and Spectroscopy Mission (XRISM)
Yao, Y., Nowak, M. A., Wang, Q. D., Schulz, N. S., & Canizares, C. R. 2008, ApJ, 672, L21
Young, A. J., Nowak, M. A., Markoff, S., Marshall, H. L., & Canizares, C. R. 2007, ApJ, 669, 830